

# Journal of Materials Chemistry B

Accepted Manuscript



This is an *Accepted Manuscript*, which has been through the Royal Society of Chemistry peer review process and has been accepted for publication.

*Accepted Manuscripts* are published online shortly after acceptance, before technical editing, formatting and proof reading. Using this free service, authors can make their results available to the community, in citable form, before we publish the edited article. We will replace this *Accepted Manuscript* with the edited and formatted *Advance Article* as soon as it is available.

You can find more information about *Accepted Manuscripts* in the [Information for Authors](#).

Please note that technical editing may introduce minor changes to the text and/or graphics, which may alter content. The journal's standard [Terms & Conditions](#) and the [Ethical guidelines](#) still apply. In no event shall the Royal Society of Chemistry be held responsible for any errors or omissions in this *Accepted Manuscript* or any consequences arising from the use of any information it contains.

# Self Assembly of plasmonic core-satellite nano-assemblies mediated by hyperbranched polymer linkers

Cite this: DOI: 10.1039/x0xx00000x

Priyanka Dey,<sup>a,b</sup> Shaoli Zhu,<sup>c</sup> Kristofer J. Thurecht,<sup>c,d</sup> Peter M. Fredericks<sup>a,b</sup> and Idriss Blakey<sup>c,d\*</sup>

Received 00th January 2012,  
Accepted 00th January 2012

DOI: 10.1039/x0xx00000x

[www.rsc.org/](http://www.rsc.org/)

The morphology of plasmonic nano-assemblies has a direct influence on optical properties, such as localised surface plasmon resonance (LSPR) and surface enhanced Raman scattering (SERS) intensity. Assemblies with core-satellite morphologies are of particular interest, because this morphology has a high density of hot-spots, while constraining the overall size. Herein, a simple method is reported for the self-assembly of gold NPs nano-assemblies with a core-satellite morphology, which was mediated by hyperbranched polymer (HBP) linkers. The HBP linkers have repeat units that do not interact strongly with gold NPs, but have multiple end-groups that specifically interact with the gold NPs and act as anchoring points resulting in nano-assemblies with a large (~48 nm) core surrounded by smaller (~15 nm) satellites. It was possible to control the number of satellites in an assembly which allowed optical parameters such as SPR maxima and the SERS intensity to be tuned. These results were found to be consistent with finite-difference time domain (FDTD) simulations. Furthermore, the multiplexing of the nano-assemblies with a series of Raman tag molecules was demonstrated, without an observable signal arising from the HBP linker after tagging. Such plasmonic nano-assemblies could potentially serve as efficient SERS based diagnostics or biomedical imaging agents in nanomedicine.

## 1. Introduction

Surface enhanced Raman scattering (SERS) is a Raman signal enhancement effect that occurs when a Raman-active molecule is present in the vicinity of a metallic surface with nanoscale roughness.<sup>1-6</sup> Since the first reports in the late 1970's, significant effort has been dedicated to developing efficient SERS substrates, comprised of noble metal nanoparticles (NPs) for various fields including electronics,<sup>7, 8</sup> understanding surface interactions,<sup>9, 10</sup> photonics,<sup>11</sup> chemical sensing,<sup>12-15</sup> biological labelling,<sup>12, 13</sup> imaging,<sup>16, 17</sup> and, more recently, as diagnostic agents for nanomedicine.<sup>3, 18, 19</sup> When Raman-active molecules are adsorbed in the interstitial gaps between NPs, also referred to as SERS "hot-spots", their Raman signals are further enhanced,<sup>1-3, 20</sup> which has motivated development of metal nano-assemblies. Colloidal nano-assemblies with nanogaps of 0-10 nm are capable of high SERS enhancements in the order of  $10^6$ - $10^{10}$  and can be relatively simple to fabricate.<sup>5</sup> These nano-assemblies have localised surface plasmon resonances (LSPR) in the visible to NIR region and the SPR maxima are strongly dependent on factors that include the assembly morphology, inter-particle separation and refractive index of the surrounding medium. In addition, the SERS intensity of nano-assemblies is also a function of its

morphology. A multitude of NP assembly morphologies<sup>4-6, 21</sup> have been investigated including dimers,<sup>22</sup> trimers,<sup>22</sup> Janus NPs,<sup>23</sup> linear nano-chains,<sup>24</sup> network arrays,<sup>25, 26</sup> spherical clusters<sup>27-29</sup> and core-satellite constructs.<sup>23, 30-33</sup> Typically, these structures have been fabricated by chemically-induced aggregation of noble metal NPs, which has involved functionalisation of the NP surface with linker molecules or macromolecules and thereafter employing electrostatic destabilisation, or linker directed self-assembly to yield nano-assemblies. The formation of such nano-assemblies has been reported with a variety of linear and branched linkers, which include DNA,<sup>34, 35</sup> antigen-antibody complexes,<sup>36</sup> organic molecules,<sup>21, 27, 37-40</sup> linear polymers,<sup>28, 41-43</sup> dendrimers<sup>26</sup> and hyperbranched polymers.<sup>22</sup> The end-group density is an important parameter for directing the self-assembly process and the resulting morphology has been shown to be dependent on the end-group density.<sup>44</sup> Branched polymeric linker molecules, such as dendrimers and hyperbranched polymers (HBP), are of particular interest, because the high end-group density can provide multiple groups to direct the assembly of NPs. While dendrimers have a precise structure, this typically comes at the expense of their synthesis requiring multiple reaction steps that often leads to low overall yields.<sup>45, 46</sup> On the other hand, while

HBPs have a less precise structure, they typically can be synthesised in a single step or via one-pot strategies with high yields and still maintain the benefit of high end-group density.<sup>47-50</sup>

We have recently reported<sup>22, 44</sup> the fabrication of varied morphologies including dimers, linear nanochains, plate-like morphologies and globular nano-assemblies by employing a HBP linker having end-groups with affinity for gold surfaces (namely, trithiocarbonate and alkyne). In these systems gold nanoparticles were coated with a sub-monolayer of HBP, so the aggregation was primarily achieved through charge destabilisation of the colloids. While some control of the size of such assemblies has been possible, the dispersity of the aggregate size was often broad and the arrangement of the NPs in the assemblies was random. A consequence of the random aggregation was that the SERS activity of the assemblies scaled with the aggregation number (i.e., number of NPs per assembly) because the hot spot density correlates directly to the assembly size in such systems. Therefore, the SERS intensity could only be increased by preparing larger assemblies, which can be undesirable for use as *in vitro* and *in vivo* biomedical imaging agents. For example, in a recent review, Liz-Marzán and co-workers<sup>6</sup> pointed out that the size of many SERS-barcoded assemblies was sufficient to either completely inhibit migration into cells, or result in the inclusion of only a very small number of “big particles”, thus decreasing the sensitivity for imaging purposes.

Core-satellite nano-assemblies have the potential to satisfy the above requirements. Ross and co-workers<sup>51</sup> have simulated the optical properties of core-satellite assemblies and demonstrated the effect of parameters including core NP diameter, satellite NP diameter, number of satellites per core NP and inter-particle distance on red-shifts of the SPR. The influence of parameters such as satellite density and inter-particle separation has also been verified experimentally.<sup>33, 51</sup> Red shift of the SPR can be important for *in vivo* applications, because it shifts the SPR into the tissue transparency window.

The different methods for generating core-satellite morphologies can be divided into two categories, namely 1) assembly mediated by complementary functionalities (e.g. complementary DNA strands,<sup>23, 52, 53</sup> metal-ligand interactions<sup>30</sup> and protein ligand interactions<sup>54</sup>) and 2) assembly mediated by multifunctional molecules, such as alkanedithiols<sup>27, 28, 49</sup> and bifunctional aromatics.<sup>31</sup> Focussing on category 2), Gandra *et al.*<sup>31</sup> have reported the formation of core-satellite clusters using *p*-aminothiophenol (*p*-ATP) as a linker molecule, where the morphology was able to be controlled by using different pH values at particular stages during self-assembly. Yoon and co-workers<sup>32, 33</sup> have used dithiol linkers (e.g. 1,10-decanedithiol) in a multi-step process that relied on the ability to selectively detach gold NPs with different sizes from a substrate. Briefly, 51 nm NPs were attached to amino-functionalised glass slides and then the particles were coated with 1,10-decanedithiol. The slides were treated with 13 nm gold NPs resulting in a surface decorated with both core-satellite assemblies and single 13 nm gold NPs. Sonication was then used to selectively detach the

core-satellite assemblies leaving single 13 nm gold NPs bound to the slide. A feature of both of these systems was that the linker molecules were densely packed in the nanogaps between the core and satellites, which limits the diffusion of small molecules into the nanogaps, which can be important for SERS substrates and barcoding assemblies with different Raman active molecules.

In this article a methodology is reported that further expands on the use of multifunctional molecules to mediate the generation of core-satellite assemblies, by using HBPs to mediate the self assembly process. HBPs synthesised by using controlled free radical polymerisation methods can be synthesised in one step, and their size, repeat unit functionality and end-group density can be tailored.<sup>47</sup> This makes them promising candidates as macromolecular linkers to form core-satellite particles, because it offers the possibility of tuning the size of the nanogap, controlling the functionality present in the nanogap and reducing the number of attachment points to the nanoparticles.

This paper reports the formation of discrete core-satellite gold nano-assemblies mediated by tailored HBP linkers with multiple end groups that bind specifically to gold nanoparticles. This was achieved by maximising the coverage of the HBP coating around core particles and then relying on unbound end-groups to sequester satellite particles that were added in a subsequent step. We investigated how the core-satellite NP stoichiometry could be varied to control the number of satellites per core and consequently what influence this had on optical properties such as LSPR maxima and SERS activity. The results were also compared to electric field simulations obtained using the finite-difference time-domain method. The core satellite assemblies were treated with a series of small molecules that had a range of Raman activities to determine whether small molecules could diffuse into the nano-gaps and whether they could be detected by SERS. These experiments also demonstrated the multiplexing capability of these core-satellite nano-assemblies which is a key requirement for application of SERS diagnostic agents in nanomedicine.

## 2. Experimental

### 2.1 Materials

Prior to use, poly(ethylene glycol) methyl ether methacrylate (PEGMA,  $\bar{M}_n=475$ ), ethylene glycol dimethacrylate (EGDMA) and 1,4-dioxane were purified by passing through a column of basic alumina. Azobisisobutyronitrile (AIBN) was recrystallised from methanol. All of the above were obtained from Sigma Aldrich. Tetrachloroauric acid and trisodium citrate were obtained from ProSciTech and used as received. Melamine, 2-naphthalenethiol, thiophenol, adenine, methylene blue and 2-quinolinethiol, deuterated chloroform ( $\text{CDCl}_3$ ) were obtained from Sigma Aldrich. Ultra-pure water ( $18 \text{ M}\Omega\text{m}^{-1}$ ) was used in all experiments.

### 2.2 Synthesis of citrate stabilised gold NPs

Gold NPs were synthesized using a variation of the methods reported by Frens<sup>55</sup> and Turkevich.<sup>56</sup> 100 mL of 0.3 mM tetrachloroauric acid was brought to boil, followed by addition of 1.6 mL or 4.3 mL of aqueous trisodium citrate solution (1 % w/v). The reaction was refluxed for a further 10 min. A colour change was observed with the initial pale yellowish solution turning pink and red respectively. The solutions of core NPs were pink having a SPR maxima at 535 nm with an average diameters of  $48 \pm 4$  nm and aspect ratio of 1.2 (by TEM). Whereas, solutions of the satellite NPs were red with a SPR maxima at 520 nm, with a diameter of  $15 \pm 1$  nm and aspect ratio of 1.05 (by TEM).

### 2.3 Synthesis of hyperbranched polymers (HBP).

The hyperbranched polymer was synthesised with polyethylene glycol methacrylate monomer as reported in our earlier publication.<sup>22</sup> Details are provided in the ESI. A schematic of the HBP has been shown in Fig. 1A. Each linear component or branch of the polymer was composed of PEGMA repeat units butyl trithiocarbonate at the  $\omega$ -end group and an alkyne at the  $\alpha$ -end group. The linear units are branched with EGDMA at random positions along the chain length. The synthesised HBP has an average of 4 branches and hence 4 trithiocarbonates (indicated in green) and 4 alkynes (indicated in red) end-groups per macromolecule. Both of these functionalities are capable of anchoring to gold surfaces<sup>57, 58</sup> and is the driving force for the nano-assembly formation.

### 2.4 Preparation of hybrid gold nano-assemblies.

A schematic of the formation of the core-satellite nano-assemblies is shown in Fig. 1B. 50  $\mu$ L of the aqueous polymer solution with a concentration of 1.5  $\mu$ M, was added with stirring to 3 mL of 0.11 nM citrate stabilised gold NPs with average diameters of 48 nm. The mixture was further stirred for at least 3 minutes and then was left standing overnight to ensure equilibrium and been reached to yield the “intermediate hybrids”. This concentration represented a 1.6 times excess when compared to the theoretical amount of polymer required to totally cover the cores (See calculation and Table S1 in ESI). It was anticipated that these intermediate NPs had free RAFT end-groups (trithiocarbonate and alkyne) available to act as anchoring points for further aggregation with additional gold NPs (see Fig. 1B). The “intermediate hybrid” colloid was centrifuged (14,500 rpm for 6 min) and the supernatant discarded to remove the unbound polymer and excess citrate. The colloid was then re-suspended in water to give 30  $\mu$ L of “intermediate hybrids” with NP concentration of  $\sim$ 100 nM. Various amounts of citrate stabilised satellite NPs (prepared by centrifugation and resuspension) were added to the pink solutions of the “intermediate hybrid” and mixed using a vortex mixer for one minute, to give a series of solutions with different mole ratios of the core and the satellite. The colloid was then allowed to stand for 3-4 hours to reach equilibrium in formation of the “core-satellite assemblies”. The core-satellite assemblies were then centrifuged (5000 rpm, 2 minutes) and the supernatant was separated to remove unbound satellite NPs.

The core-satellite assemblies were then diluted with ultrapure water to give a primary NP concentration of  $\sim$ 2 nM. These samples were then analysed by UV-vis spectroscopy, and also used for SERS, DLS and TEM analysis.

## 2.5 Characterisation

### 2.5.1 UV-VISIBLE SPECTROSCOPY

Ultraviolet-visible spectra were acquired using a Varian Cary 50 in the range of 400-900 nm with a 1 cm path length cell, with baseline correction.

### 2.5.2 DYNAMIC LIGHT SCATTERING (DLS)

DLS measurements were performed using a Malvern Zetasizer Nano Series running DTS software and a 4 mW He-Ne laser at 633 nm. Analysis was performed at an angle of  $90^\circ$  and a constant temperature of  $25^\circ\text{C}$ . Dilute NP concentrations were used to ensure that multiple scattering and particle-particle interactions could be considered to be negligible.

### 2.5.3 TRANSMISSION ELECTRON MICROSCOPY (TEM)

A JEOL 1400 transmission electron microscope was used to study the size and morphology of the nano-assemblies deposited on 200 mesh holey C-coated copper grids at 100 keV. As-prepared hybrid samples were diluted 100-fold, in order to minimise the drying artefacts and deposited on TEM grids. ImageJ software was used for calculating the number of satellites per core NP by analysing  $\sim$ 63-92 individual assemblies per sample. For selected samples TEM images were also acquired at  $3^\circ$  tilt intervals over  $120^\circ$  resulting in 40 images of an individual nano-assemblies. The images were captured by SerialEM software and processed by IMOD software to obtain a video and 3D-tomographic model of the core-satellite assemblies.

### 2.5.4 RAMAN SPECTROSCOPY

SERS spectra of the linker HBP of colloidal assemblies were recorded in the spectral range  $200\text{--}2000\text{ cm}^{-1}$  for 4 accumulations of 40 s each. SERS spectra of the colloidal assemblies for multiplexing were recorded in the spectral range  $200\text{--}3200\text{ cm}^{-1}$  for 5 accumulations of 10 s each. A Renishaw model InVia microRaman spectrometer equipped with a 785 nm excitation from a diode laser, a single diffraction grating and an electrically cooled CCD detector was used. The laser power was 20 mW at the sample. Low volume quartz cuvettes were used as sample holders.

### 2.6 Electromagnetic field distribution simulations.

The electromagnetic field intensity distribution around the nanostructures was simulated using a three dimensional finite-difference time-domain (FDTD) method. FDTD is a powerful computational method which is widely used to calculate the electromagnetic properties of different materials. It treats Maxwell equations as a set of finite differential equations in both time and space. The model space considered included both the probe and the sample surface and consisted of an array of

cubic cells (Yee cells) with each cell having its own complex dielectric constant. The FDTD Solutions software package (Lumerical Solutions Inc, Vancouver Canada) was used to carry out the computational calculations and numerical analysis. The incident light was *p*-polarized. The mesh size in the *x*, *y* and *z* directions was  $\Delta x = 1$  nm,  $\Delta y = 1$  nm and  $\Delta z = 1$  nm, respectively. The simulation time, *t*, was 100 fs. Perfectly matched layer (PML) absorbing boundary conditions were selected in three directions. A core gold NP with a diameter of 50 nm surrounded by varying numbers of satellite NPs (0, 1, 5 and 8) with a diameter of 15 nm was simulated. The distance between the core and its satellites was set to 2 nm.

### 3. Results and discussion

#### 3.1 Hyperbranched polymer

The overall approach that has been used for formation of core-satellite nano-assemblies is shown in Fig. 1. Hyperbranched polymers (HBPs) (see Fig. 1A) were coated around gold nanoparticles and unbound end-groups in this layer were used to mediate the self assembly of satellite particles that were added subsequently (see Fig. 1B).

The HBP was synthesised in a single step that involved reversible addition fragmentation chain-transfer (RAFT) polymerisation<sup>59</sup> of polyethylene glycol methacrylate using ethylene glycol dimethacrylate to facilitate branching. This produced a HBP with a hydrodynamic diameter ( $D_h$ ) of  $8.5 \pm 2$  nm,  $M_w$  of 100 kDa and an average of 4 branches, which resulted in an average of 8 functional end-groups, that is, 4 trithiocarbonate end-groups and 4 alkyne end-groups.<sup>22</sup> RAFT polymerisation allows incorporation of functional end-groups into the structure, which were derived from the RAFT agent and in this case the required end-groups could be introduced during polymerisation and subsequent post-modification reactions were not required. These HBPs are primarily comprised of polyethylene glycol methacrylate repeat units, which do not strongly bind to gold NPs. However, the

trithiocarbonate and alkyne containing end groups have a strong affinity for binding to gold surfaces.<sup>57, 58</sup>

#### 3.2 Synthesis and optical characterisation of gold NPs with different sizes for use as cores and satellites.

In order to understand the mechanism of self-assembly of the core-satellite nano-assemblies, gold NPs with two different diameters were prepared using modified versions of the methods reported by Frens<sup>55</sup> and Turkevich,<sup>56</sup> where the mole ratio of sodium citrate to gold (III) was varied to achieve different particle sizes. The TEM micrograph in Fig. 2A shows NPs with average diameters of  $48 \pm 4$  nm and an aspect ratio of 1.2 were prepared. These particles were subsequently used as the core NPs. Fig. 2B shows TEM micrographs of particles that have average diameters of  $15 \pm 1$  nm and an aspect ratio of 1.05; these particles were later used as the satellites. The visible spectra of aqueous solutions of the NPs are shown in Fig. 2C demonstrating that the 48 nm core NPs had a SPR maximum at 535 nm, while the 15 nm satellite NPs had a SPR maximum at 520 nm, which is typical for gold NPs of these sizes.<sup>60</sup> Based on the average particle sizes and the amount of gold salt added during synthesis, the calculated NP concentrations for the 48 and 15 nm NPs were 0.11 nM and 3.5 nM respectively.

#### 3.3 Effect of stoichiometry of satellite and core NPs on the morphology of core-satellite nano-assemblies.

The first step in the self assembly process was to form “intermediate hybrids” that ultimately formed the core of the assemblies. This was achieved by coating the 48 nm gold NPs with HBP using a ligand exchange mechanism. A high degree of coverage of the particle with HBP was achieved by using an excess of polymer (calculation shown in ESI), where the unbound polymer was removed by centrifugation. Resuspension of the centrifuged intermediate hybrids resulted in a primary particle concentration of approximately 100 nM. The next step involved mixing the “intermediate hybrids” with varying mole ratios (0-100) of the 15 nm citrate stabilised

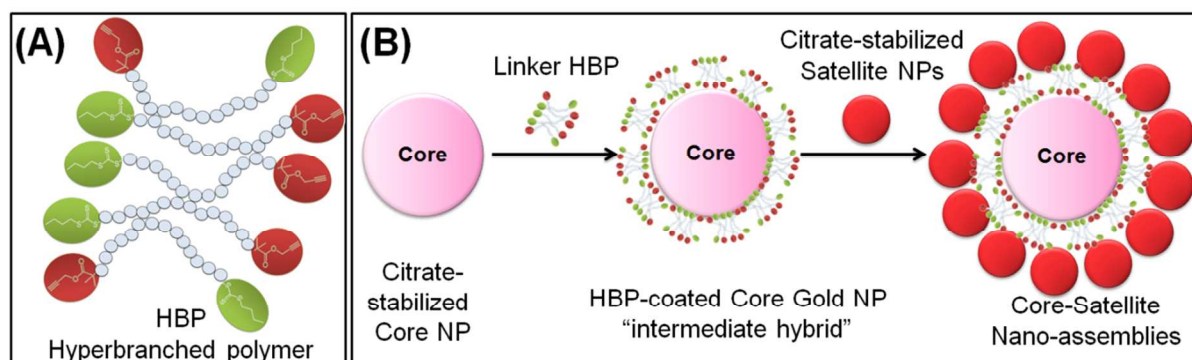


Fig. 1. (A) Stylised representation of the hyperbranched polymer (HBP) linker showing the two types of anchoring end-groups, namely, trithiocarbonate in green and alkyne in red, and (B) a schematic showing the formation of core-satellite nano-assemblies mediated by linker HBP with larger gold NPs as the core and smaller NPs as the satellites.

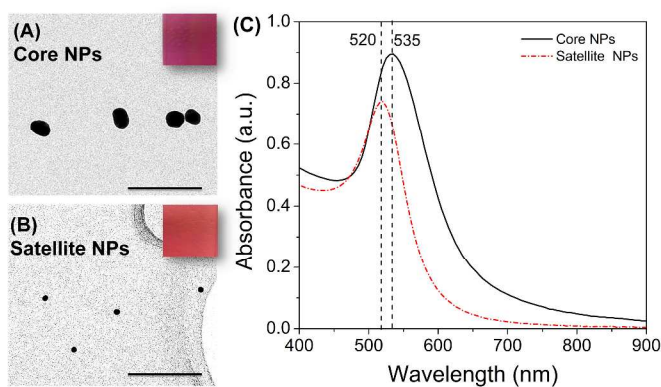


Fig. 2. (A) TEM micrograph of gold NPs with average diameters of  $48 \pm 4$  nm, which were subsequently used as the core NP, and (B) TEM micrograph of gold NPs with average diameters  $15 \pm 1$  nm which were subsequently used as the satellite NPs. The inset shows the color of the colloids. TEM scale bar = 200 nm. (C) Visible spectra of the core and satellite NPs.

gold nanoparticles. These particles were expected to anchor to any unbound end-groups present on the HBP coating of the intermediate hybrid, thus forming core-satellite nano-assemblies. Smaller NPs were used as satellites, because they allow a larger number of satellites per core NP and therefore a larger number of NP junctions or potential hot-spots. Many of the approaches that have been reported for formation of core-satellite nano-assemblies are based on complimentary recognition<sup>23, 30, 52-54</sup> and hence require functionalisation of both core and satellites, which was not a requirement in our approach, thus making it a simpler method.

To determine the morphology of the assemblies, conventional TEM micrographs were acquired for each of the satellite-core mole ratios used and representative examples are shown in Fig. 3 (column 1). Plots showing the distribution in the number of satellites per core that are visible by conventional TEM have also been shown (see Fig. 3, column 2). Qualitatively it can be seen that the number of satellites per core NP increases as a function of the satellite-core mole ratio used in the self-assembly process. Combining the data of Fig. 3 (column 2), the number of visible satellites per core NP (averaged value from 63-92 nano-assemblies per sample from conventional TEM) has been plotted with respect to the satellite-core NP stoichiometry in Fig. 4. The median number of visible satellites per core NP was observed to dramatically increase with an increase in NP stoichiometry from 0 to 30, followed by a less pronounced increase thereafter. With a mole ratio of 5, lower order assemblies of monomers and dimers (0-1 satellites per core NP) were observed, whereas, higher order nano-assemblies of 3-4 satellites per core NP were formed with a mole ratio of 15. Upon increasing the mole ratio from 15 to 30, a significant increase in the satellite density per core NP from approximately 4 to 8 was observed. On further increasing the satellite-core mole ratio, the number of satellites surrounding the core increased slightly from  $8 \pm 1$  to  $10 \pm 1$  for satellite-core ratios of 30 and 100 respectively. The maximum number of visible satellites per core NP that was observed by

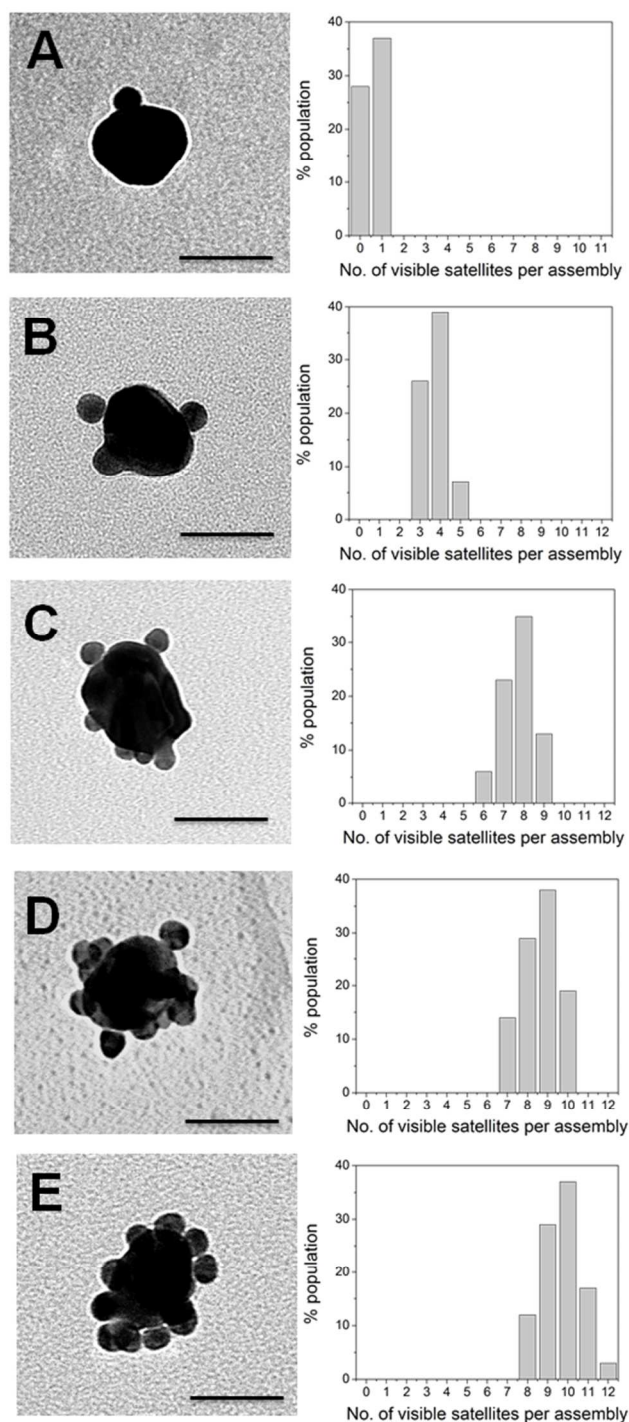


Fig. 3. TEM micrographs of core-satellite nano-assemblies (column 1), together with their TEM derived statistical population of visible satellite density per core NP (column 2), with increasing satellite-core mole ratios of (A) 5, (B) 15, (C) 30, (D) 50, and (E) 100. Scale bar = 50 nm

TEM was  $10 \pm 1$ . According to Song and co-workers<sup>61</sup> a maximum of 63.4% of the surface area of the core will be covered with satellites for random close packing of satellites. Therefore, when taking this into account and then considering the surface area of the core and the area that

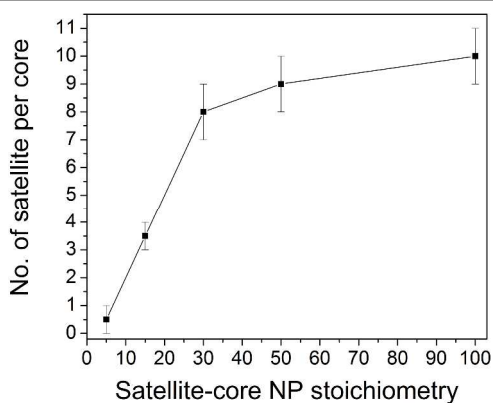


Fig. 4. Plot of median number of visible satellites per core NP with respect to satellite-core NP stoichiometry i.e., satellite to core mole ratio.

a satellite will cover, theoretically, the maximum number of satellites per core is expected to be approximately 50.

Conventional TEM measurements are based on transmission of electrons through the assemblies, so only clearly show the satellite NPs that extend past the periphery of the core NP, however, rotation of the TEM stage allows visualisation of the obscured satellites. To demonstrate this phenomenon TEM images were acquired for the assemblies formed using satellite-core mole ratios of 30 and 100, through a total tilt of  $120^\circ$  at regular intervals of  $3^\circ$ . A selection of TEM micrographs at incremental rotations of  $30^\circ$  are shown in Figs. 5A and B. 5-6 satellites can be observed in the TEM micrographs for the different rotations shown in Fig. 5A, for a mole ratio of 30, but the 3D reconstruction reveals that at least 7 satellites are present. Similarly, 6-8 satellites could be observed for different rotations (Fig. 5B), for a mole ratio of 100, but the 3D reconstruction in Fig. 5D reveals that at least 10 satellites are present. These results indicate that some of the satellites will not be visible in conventional TEM images and show that as many as 40% of satellites can be obscured. Taking the obscured areas of the particles in the conventional TEM analysis into account, the maximum number of satellites achieved would be approximately 15, which is still considerably less than the theoretical maximum of 50. The lower density of satellites is likely due to the negative charge of the citrate stabilised satellite NPs, which causes repulsion between the satellites and will restrict close packing of satellites on the core and also inhibit formation of satellite-satellite NP junctions.

The gap separating the satellite and core NPs will also be important in dictating the SERS intensity. The series of TEM micrographs at various angles of tilt that were described above revealed that the average separation between the core and satellites was  $1.2 \pm 0.4$  nm. The median size of the HBP linker, when dissolved in water, was approximately 8.5 nm (by DLS). This disparity is probably due to distortion of the polymer conformation that results from anchoring to NP surfaces and

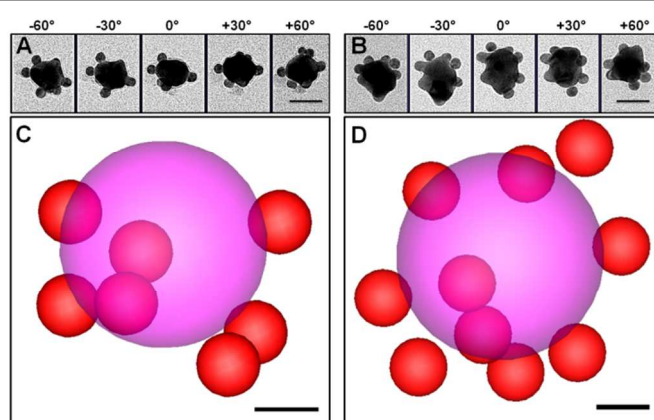


Fig. 5. Tilt-TEM images at  $30^\circ$  tilt intervals for core-satellite nano-assemblies of mole ratios of (A) 30 and (B) 100. 3D tomographic reconstruction of core-satellite assemblies prepared using core-satellite mole ratios of (C) 30 and (D) 100. Core NP shown in pink and satellite NP shown in red. Scale bars = 50 nm for A and B and 13 nm for C and D.

also the dehydration of the polymer upon drying on the TEM grid.

The average sizes of the colloids in solution was also assessed by DLS. The gold NPs that were used as the core particles had diameters of  $65 \pm 10$  nm and the gold NPs that were used as satellites had diameters of  $18 \pm 5$  nm.<sup>†</sup> The nanoassemblies prepared using a satellite-core mole ratio of 5 had median diameters of approximately  $95 \pm 9$  nm while the other mole ratios (15-100) had median diameters of  $105 \pm 15$  nm. Within experimental error, these results were consistent with the formation of core-satellite nano-assemblies rather than large aggregates.

### 3.4 Optical properties of the core-satellite nano-assemblies.

The visible spectra and photographs of the assembled colloids after centrifugation and re-suspension in water are shown in

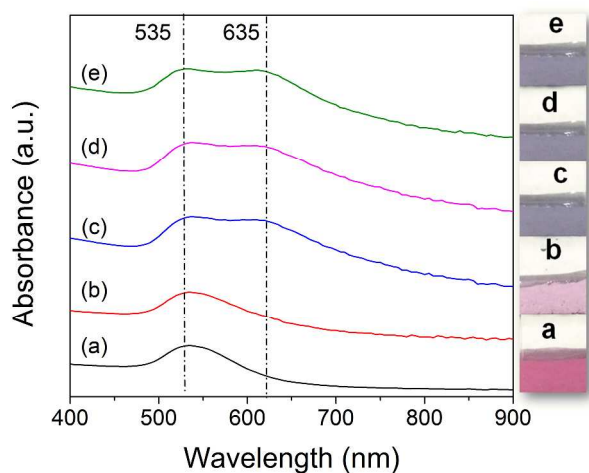


Fig. 6. Visible spectra of core-satellite assemblies prepared using satellite-core mole ratios of (a) 5, (b) 15, (c) 30, (d) 50, and (e) 100. The spectra are offset by 0.25 a.u.

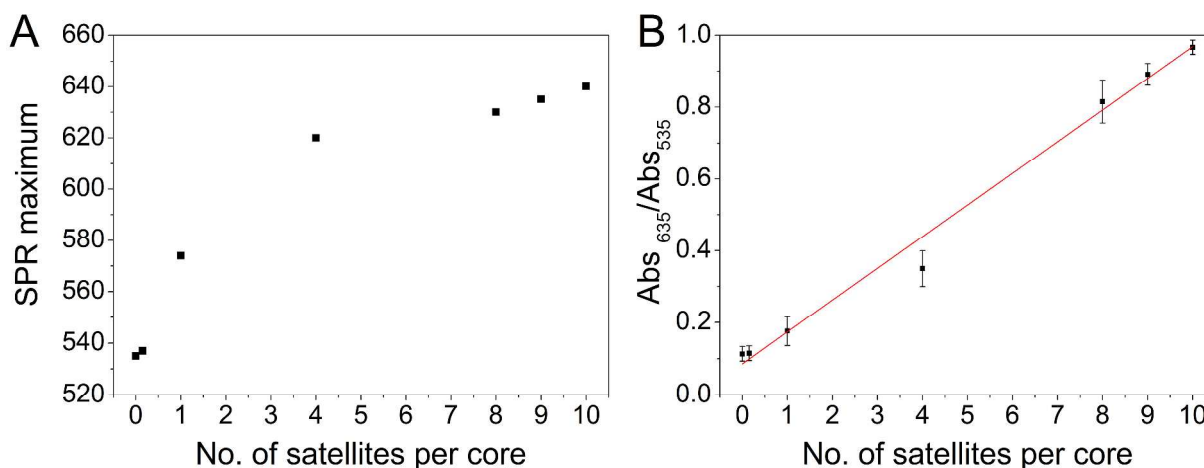


Fig. 7. Plot of (A) SPR maximum versus number of satellites per core, and (B) SPR absorbance ratio of 635 to 535 nm ( $Abs_{635}/Abs_{535}$ ), with respect to the number of satellites per core.

Fig. 6. The core NPs and intermediate hybrids had SPR maxima at 535 nm and 537 nm respectively (shown as the 2 data points at a mole ratio of 0 in Fig. 7A and B). The red-shift of  $\sim 2$  nm for the intermediate hybrids is probably due to the increase in the refractive index of the surrounding media, due to the presence of the polymer coating.<sup>62</sup> After normalisation of the visible spectra and spectral subtraction of the core NP spectrum, we obtained SPR maxima for each of the mole ratios used. The plot in Fig. 7A demonstrates that the SPR shifts to the red with an increasing number of satellites per core NP. The maximum SPR shift achieved was 105 nm for nano-assemblies with an average of 10 satellites per core. These results are consistent with the simulations reported by Ross and co-workers, which showed that the SPR is predicted to red-shift with increasing numbers of satellite particles.<sup>51</sup> We also studied the ratio of the absorbance at 635 nm and 535 nm

( $Abs_{635}/Abs_{535}$ ) as a function of the number of satellites per core NP (see Fig. 7B), which demonstrated a linear dependence. Therefore, it was concluded that the optical characteristics of the core-satellite nano-assemblies specifically, the SPR shift and the absorbance ratio, is a direct function of the number of satellites per core NP.

### 3.5 SERS activity of core-satellite nano-assemblies.

It has been well documented in the literature that high Raman signal intensities are obtained from higher order assemblies i.e., for high hot-spot densities.<sup>5</sup> Hence, the SERS performance not only acts as a means to characterize the extent of aggregation and hot-spot density, but also the nano-assemblies to be tailored to achieve higher SERS efficiencies. A typical HBP SERS spectrum from the nano-assemblies at a concentration of 2 nM

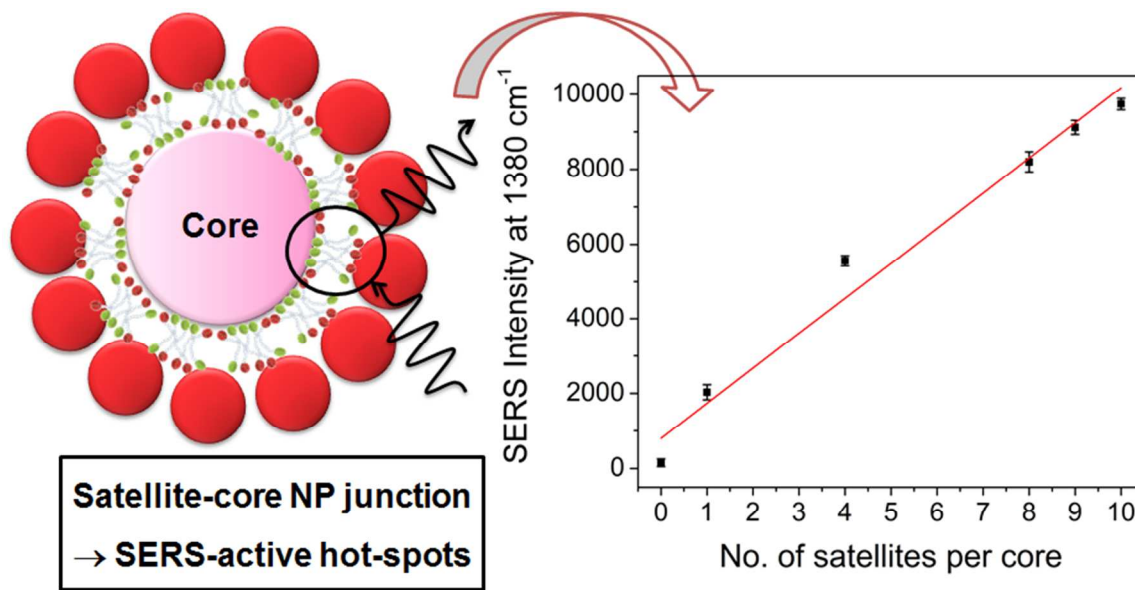


Fig. 8. Plot of SERS intensity at  $1380\text{ cm}^{-1}$  due to linker HBP versus the number of satellites per core NP, together with a cartoon of the core-satellite nano-assembly showing schematically the location of the HBP-containing SERS-active hot-spots. The concentration of nanoassemblies was 2 nM.

is shown in Fig. S3 in the ESI. The peak at  $1380\text{ cm}^{-1}$  was assigned to  $\delta(\text{CH}_3)$  from the p(PEGMA), while the peaks at  $1022\text{ cm}^{-1}$  and  $800\text{ cm}^{-1}$  were assigned to the  $\nu(\text{C}=\text{S})$  and  $\nu(\text{C}-\text{S})$  modes respectively, which can be attributed to the trithiocarbonate end-groups. The SERS of the HBP present between the satellite-core junctions provides a good insight into the relative number of SERS-active hot-spots of the nano-assemblies (see cartoon in Fig. 8). As discussed earlier, satellite-satellite junctions are unlikely to be formed and hence their contribution towards SERS can be considered negligible. The intensity of the peak at  $1380\text{ cm}^{-1}$  was plotted with respect to the number of satellites per core, and is shown in Fig. 8. The intermediate hybrid (acting as the reference sample, 0 mole ratio) did not show any observable SERS signal due to the HBP. This shows that the signal enhancement afforded by a single gold NP with a diameter of 48 nm is insufficient for detecting HBP at a concentration of  $\sim 10^{-9}\text{ M}$ . In contrast, the core-satellite nano-assemblies were able to detect the HBP in this concentration range, and highlights the very high SERS activity of these systems. Fig. 8 shows a linear increase in SERS intensity with the increase in the number of satellites per core. The data reported were averaged from the SERS intensities of three separate batches and was measured at three positions for each sample. It can be seen that the variance of the values, indicated by the error bars, is low. This low standard deviation of the SERS intensities demonstrates the good reproducibility of SERS of the assemblies.

To investigate this further, finite-difference time-domain (FDTD) simulations were performed to estimate the electric field intensity for core-satellite assemblies with varying numbers of satellite NPs (see Fig. 9A). The core NPs with no satellites have a very low electric field intensity ( $|E|^2$ ) at the surface of the particle (Fig. 9A a) when compared to those

decorated with satellite NPs, which exhibit a high electric field intensity in the gap between the core and satellite NPs (Fig. 9A b-d) and the highest intensities are observed for the gaps that coincide with the direction of polarization. When the electric field intensity was integrated for the morphologies, a linear relationship was observed with the number of satellites, which is consistent with the linear increase in SERS intensity with number of satellites that was observed experimentally (as shown in Fig. 8). These core-satellite nano-assemblies show evidence of a significant degree of control of the morphology, size, satellite density and hot-spot density, providing us with tunable SERS enhancements. Such tailor-made nano-assemblies exhibit potential for applications as plasmonic bio-sensors in various fields including electronics, catalysis and medical diagnostics.

### 3.6 Multiplexing of core-satellite nano-assemblies.

Both fluorescence based quantum dots<sup>63</sup> and SERS based gold NPs<sup>64</sup> have shown great potential as multiplexed diagnostics and biomedical imaging agents. For successful translation of these diagnostic agents for use in *ex vivo* or *in vivo* conditions, key requirements include negligible auto-fluorescence in the tissue NIR window, low cytotoxicity, multiplexing capability simultaneous detection of different “tags” or signatures and limited or no photo-bleaching.<sup>3, 12, 18, 19, 65</sup> Gold NP based SERS agents comply with all the above requirements and hence are well suited for biomedical applications.<sup>13, 66</sup> As demonstrated earlier, the tailored core-satellite nano-assemblies have high hot-spot densities and strong SERS scattering. Therefore, the capability of multiplexing of the core-satellite assemblies was investigated with six different commercially available Raman tag molecules.

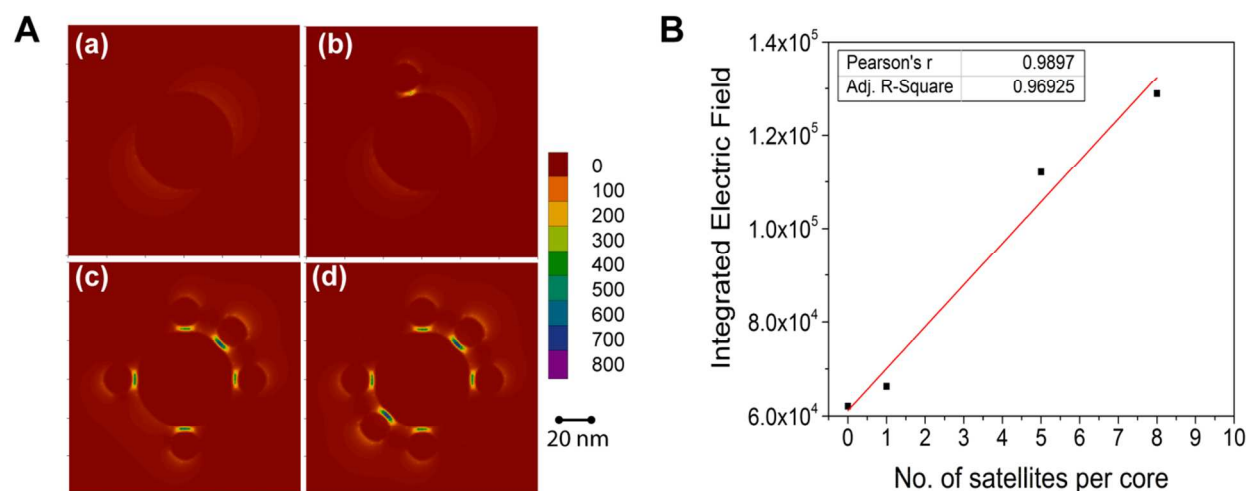


**Fig. 9.** (A). FDTD simulation showing the electric field intensity ( $|E|^2$ ) of core-satellite nano-assemblies with (a) 0, (b) 1, (c) 5, and (d) 8 satellites per core NP. The direction of polarisation is approximately  $+45^\circ$  from the vertical. (B). Plot of integrated electric field from the calculations of FDTD simulation study with respect to the number of satellites per core NP.

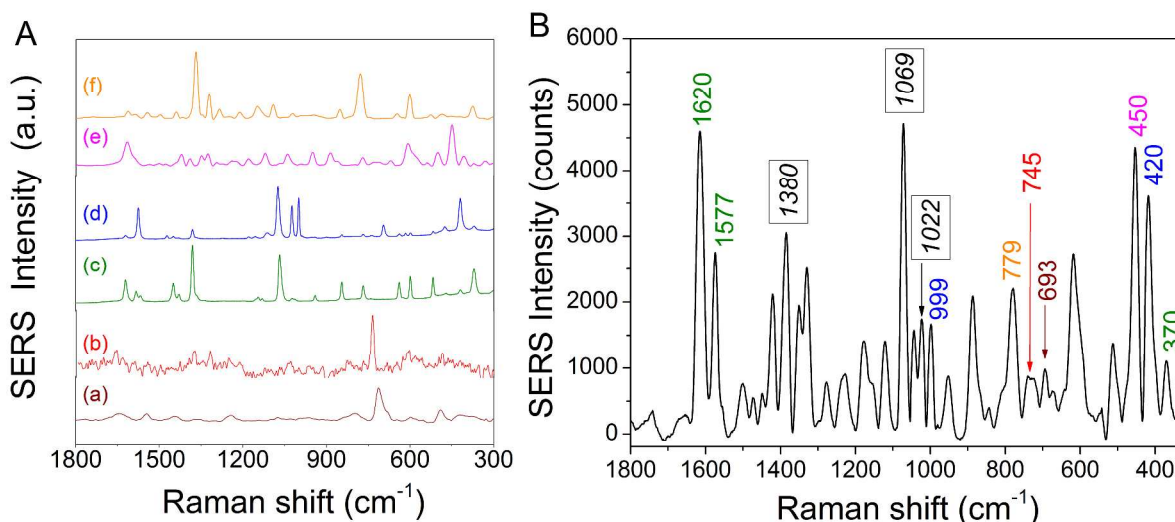


**Fig. 10.** (A) SERS spectra of core-satellite assemblies tagged with (a) melamine, (b) adenine, (c) 2-naphthalenethiol, (d) thiophenol, (e) methylene blue, and (f) 2-quinolinethiol. The spectra have been normalised so as to make the characteristic peaks prominent. (B) SERS spectrum of a mixture of core-satellite nano-assemblies labelled six different tags (a-f). The ratios of the nanoassemblies were adjusted according to the SERS efficiency of the tag molecules. Same colours have been used to indicate the non-overlapping characteristic peaks of the tag molecules in B as was used for their individual spectra in A.

The tag molecules selected possessed amine or thiol functionalities, which allows them to anchor to the gold NPs. They also constituted a broad range of Raman scattering cross-sections, i.e., low, medium and high Raman signal intensity per unit concentration. The Raman tags were added to separate aliquots of the core-satellite nano-assemblies and their SERS spectra acquired using an excitation line of 785 nm (see Fig. 10A). Melamine and adenine had lower SERS signal intensities (Fig. 10A (spectrum a, b)) compared with the high intensity signals obtained from 2-naphthalenethiol, 2-quinolinethiol and thiophenol (Fig. 10A (spectrum c, f, d)). Methylene blue showed intermediate SERS intensities (Fig. 10A (spectrum e)). These results demonstrated that the core-satellite nano-assemblies could be barcoded with a number of different Raman tag molecules. It should be noted that no peaks due to the HBP were observed after addition of the tag molecules. The HBP concentration ( $\sim 10^{-9}$  M) was at least two orders of magnitude lower than that employed for the Raman tag molecules ( $\sim 10^{-7}$  M), thus the SERS spectrum of the HBP from the nano-assemblies was overwhelmed with that of the tag molecule and did not cause interference in detection of the tags. This suggests it is possible for small molecules to diffuse into the nano-gap and that the HBP linker will not interfere with analyte detection for analyte concentrations as low as  $10^{-7}$  M, an important criterion for usefulness of SERS nano-assemblies as chemical sensors. It also demonstrates an advantage of using HBPs as the linker when compared to small molecules linkers. For example Yoon and coworkers,<sup>32, 33</sup> used 1,10-decanedithiol to mediate formation of core-satellite particles. For such a system it would be expected that a dense monolayer of thiols would be present which would limit the entry of analytes in to the nano-gap and indeed they only reported observing a SERS signal from mono-thiols that were added at the same time as the alkanedithiol, i.e. during formation of the nanoassemblies. For

the systems in our study the HBP provides multiple end groups to facilitate self assembly, but the confirmation of the polymer facilitates entry of analyte or tag molecules after self assembly.

The individually barcoded colloidal nano-assemblies were combined into a single multiplexed colloid where six types of barcoded assemblies co-existed. The SERS spectrum of the multiplexed core-satellite assemblies was analysed and the six different individual barcodes were recognised by detecting the non-overlapping characteristic peaks. The individual tags had different Raman scattering efficiencies and hence the tag molecule concentrations were adjusted accordingly in the multiplexed sample. The multiplexed spectrum in Fig. 9B shows the presence of melamine (characteristic peak at  $693\text{ cm}^{-1}$ ), adenine (characteristic peak at  $745\text{ cm}^{-1}$ ), 2-naphthalenethiol (characteristic peaks at  $1620$ ,  $1577$  and  $370\text{ cm}^{-1}$ ), thiophenol (characteristic peaks at  $999$ ,  $420\text{ cm}^{-1}$ ), methylene blue (characteristic peak at  $450\text{ cm}^{-1}$ ), and 2-quinolinethiol (characteristic peak at  $779\text{ cm}^{-1}$ ). The peaks at  $1380$ ,  $1022$  and  $1069\text{ cm}^{-1}$  were common to more than one Raman tag molecule and hence have not been used as identifying peaks for the barcodes in the multiplexed spectrum. These results confirm that the core-satellite assemblies can be easily multiplexed with a variety of Raman tag molecules, thereby making them ideal candidates for development of SERS-based diagnostics or biomedical imaging agents in nanomedicine.

#### 4. Conclusions

The formation of core-satellite plasmonic nano-assemblies was investigated, where the self assembly was mediated by hyperbranched polymer linkers which had multiple end-groups that could specifically bind to gold nanoparticles. Gold particles that would ultimately constitute the core were coated with HBP, such that the coverage was maximised using an excess of the polymer and then purified by centrifugation. The unbound end-

groups on the HBP coating the 'intermediate hybrids' were then used to sequester satellite particles. The core-satellite morphology was confirmed by conventional TEM, as well as reconstruction of TEM micrographs at various tilt angles. These results also revealed that the density of satellites was dependent on the mole ratio of the satellite to core NPs used during the self-assembly and began to level off for ratios above 30. This result was also supported by the FDTD simulation studies. We observed that the optical characteristics of the nano-assemblies including the SPR shift and the SPR absorbance ratios were a direct function of the number of satellites per core NP. Hence, the ability to control the satellite density gives the capability to control the SERS-active hot-spot density and thereby tune the SERS performance. Evidence was also provided that our core-satellite nano-assemblies have the potential to be used as multiplexed imaging agents by demonstrating SERS spectra could be obtained from after six commercially available SERS tag molecules were allowed to diffuse into the hot spots. It should also be noted that assemblies could be easily be detected at concentrations of 2 nM. Thus, these SERS-active core-satellite nano-assemblies, having tunable SPR and hot-spot density along with useful multiplexing capability, could potentially serve as SERS diagnostic or imaging agents in nanomedicine.

### Acknowledgements

This research was supported under the Australian Research Council (ARC) Discovery Projects Scheme (project number DP1094205). IB and KJT would also like to acknowledge the ARC for Future Fellowship funding (FT100100721, FT110100284). This work was performed in part at the Queensland node of the Australian Microscopy and Microanalysis Research Facility (AMMRF) within the Central Analytical Research Facility (CARF) at Queensland University of Technology. We would also like to acknowledge Dr. Jamie Riches for assistance with the tilt-TEM and 3D model reconstruction studies. Thanks are also due to Dr. Llewellyn Rintoul for assistance in obtaining Raman spectra and Dr. Craig Bell for providing us with the precursors for the RAFT agent.

### Notes and references

<sup>a</sup> School of Chemistry, Physics and Mechanical Engineering, Queensland University of Technology, Brisbane, Queensland 4001, Australia.

<sup>b</sup> Institute of Future Environments, Queensland University of Technology, Brisbane, Queensland 4001, Australia.

<sup>c</sup> Australian Institute of Bioengineering and Nanotechnology, University of Queensland, St. Lucia, Queensland 4072, Australia.

<sup>d</sup> Centre for Advanced Imaging, University of Queensland, St. Lucia, Queensland 4072, Australia.

† It should be noted that the sizes obtained by DLS are typically biased towards the larger particles in the distributions and hence are slightly higher than those obtained by TEM.

Electronic Supplementary Information (ESI) available: Preparation and characterisation of nano-assemblies- effect of linker HBP coverage, calculation of HBP coverage on core gold NPs, visible spectra of core-satellite nano-assemblies along with the photographs of the colloid- effect

of HBP coverage and SERS spectrum of HBP residing in the hot-spots of the core-satellite assemblies are included. See DOI: 10.1039/b000000x/

1. R. Jin, *Angew. Chem. Int. Ed.*, 2010, **49**, 2826–2829.
2. X. M. Lin, Y. Cui, Y. H. Xu, B. Ren and Z. Q. Tian, *Anal. Bioanal. Chem.*, 2009, **394**, 1729–1745.
3. K. C. Bantz, A. F. Meyer, N. J. Wittenberg, H. Im, O. Kurtulus, S. H. Lee, N. C. Lindquist, S.-H. Oh and C. L. Haynes, *Phys. Chem. Chem. Phys.*, 2011, **13**, 11551–11567.
4. H. Ko, S. Singamaneni and V. V. Tsukruk, *Small*, 2008, **4**, 1576–1599.
5. S. L. Kleinman, R. R. Frontiera, A.-I. Henry, J. A. Dieringer and R. P. v. Duyne, *Phys. Chem. Chem. Phys.*, 2013, **15**, 21–36.
6. J. M. Romo-Herrera, R. A. Alvarez-Puebla and L. M. Liz-Marzán, *Nanoscale*, 2011, **3**, 1304–1315.
7. J. Herrmann, K. H. Müller, T. Reda, G. R. Baxter, B. Raguse, G. J. J. B. d. Groot, R. Chai, M. Roberts and L. Wiczorek, *Appl. Phys. Lett.*, 2007, **91**, 183105.
8. S. Paul, C. Pearson, A. Molloy, M. A. Cousins, M. Green, S. Kolliopoulou, P. Dimitrakis, P. Normand, D. Tsoukalas and M. C. Petty, *Nano Lett.*, 2003, **3**, 533–536.
9. I. Blakey, Z. Merican, L. Rintoul, Y.-M. Chuang, K. S. Jack and A. S. Micallef, *Phys. Chem. Chem. Phys.*, 2012, **14**, 3604–3611.
10. I. Blakey, T. L. Schiller, Z. Merican and P. M. Fredericks, *Langmuir*, 2010, **26**, 692–701.
11. J. R. Adleman, D. A. Boyd, D. G. Goodwin and D. Psaltis, *Nano Lett.*, 2009, **9**, 4417–4423.
12. S. Liu and Z. Tang, *J. Mater. Chem.*, 2010, **20**, 24–35.
13. M.-C. Daniel and D. Astruc, *Chem. Rev.*, 2004, **104**, 293–346.
14. Y. Xie, X. Wang, X. Han, X. Xue, W. Ji, Z. Qi, J. Liu, B. Zhao and Y. Ozaki, *Analyst*, 2010, **135**, 1389–1394.
15. X. X. Han, G. G. Huang, B. Zhao and Y. Ozaki, *Anal. Chem.*, 2009, **81**, 3329–3333.
16. M. De, P. S. Ghosh and V. M. Rotello, *Adv. Mater.*, 2008, **20**, 4225–4241.
17. P. Dey, W. Olds, I. Blakey, K. J. Thurecht, E. L. Izake and P. M. Fredericks, *J. Raman Spectrosc.*, 2013, **44**, 1659–1665.
18. X. Qian, X. H. Peng, D. O. Ansari, Q. Y. Goen, G. Z. Chen, D. M. Shin, L. Yang, A. N. Young, M. D. Wang and S. Nie, *Nat. Biotechnol.*, 2008, **26**, 83–90.
19. R. A. Alvarez-Puebla and L. M. Liz-Marzán, *Small*, 2010, **6**, 604–610.
20. L. Guerrini and D. Graham, *Chem. Soc. Rev.*, 2012, **41**, 7085–7107.
21. Q. Ji, S. Acharya, J. P. Hill, G. J. Richards and K. Ariga, *Adv. Mater.*, 2008, **20**, 4027–4032.
22. P. Dey, I. Blakey, K. J. Thurecht and P. M. Fredericks, *Langmuir*, 2013, **29**, 525–533.
23. H. Xing, Z. Wang, Z. Xu, N. Y. Wong, Y. Xiang, G. L. Liu and Y. Lu, *ACS Nano*, 2012, **6**, 802–809.
24. H. Jia, X. Bai, N. Li, L. Yua and L. Zheng, *CrystEngComm*, 2011, **13**, 6179–6184.
25. A. Y. Koyfman, G. Braun, S. Magonov, A. Chworos, N. O. Reich and L. Jaeger, *J. Am. Chem. Soc.*, 2005, **127**, 11886–11887.
26. S. Srivastava, B. L. Frankamp and V. M. Rotello, *Chem. Mater.*, 2005, **17**, 487–490.

27. H. Yan, S. I. Lim, L. C. Zhang, S. C. Gao, D. Mott, Y. Le, R. Loukrakpam, D. L. An and C. J. Zhong, *J. Mater. Chem.*, 2011, **21**, 1890-1901.
28. A. K. Boal, F. Ilhan, J. E. DeRouchey, T. Thurn-Albrecht, T. P. Russell and V. M. Rotello, *Nature* 2000, **404**, 746-748.
29. L. A. Connal, N. A. Lynd, M. J. Robb, K. A. See, S. G. Jang, J. M. Spruell and C. J. Hawker, *Chem. Mater.*, 2012, **24**, 4036-4042.
30. I. Choi, H. D. Song, S. Lee, Y. I. Yang, T. Kang and J. Yi, *J. Am. Chem. Soc.*, 2012, **134**, 12083-12090.
31. N. Gandra, A. Abbas, L. Tian and S. Singamaneni, *Nano Lett.*, 2012, **12**, 2645-2651.
32. J. H. Yoon, J. Lim and S. Yoon, *ACS Nano*, 2012, **6**, 7199-7208.
33. J. H. Yoon, Y. Zhou, M. G. Blaber, G. C. Schatz and S. Yoon, *J. Phys. Chem. Lett.*, 2013, **4**, 1371-1378.
34. A. P. Alivisatos, K. P. Johnsson, X. G. Peng, T. E. Wilson, C. J. Loweth, M. P. Bruchez and P. G. Schultz, *Nature*, 1996, **382**, 609-611.
35. J. Loweth, W. B. Caldwell, X. G. Peng, A. P. Alivisatos and P. G. Schultz, *Angew. Chem. Int. Ed.*, 1999, **38**, 1808-1812.
36. S. Basu, S. K. Ghosh, S. Kundu, S. Panigrahi, S. Praharaj, S. Pande, S. Jana and T. Pal, *J. Colloid Interf. Sci.*, 2007, **313**, 724-734.
37. R. Kaminker, M. Lahav, L. Motiei, M. Vartanian, R. Popovitz-Biro, M. A. Iron and M. E. v. d. Boom, *Angew. Chem. Int. Ed.*, 2010, **49**, 1218-1221.
38. M. M. Maye, J. Luo, I. S. Lim, L. Han, N. N. Kariuki, D. Rabinovich, T. Liu and C. J. Zhong, *J. Am. Chem. Soc.*, 2003, **125**, 9906-9907.
39. Z. Shen, M. Yamada and M. Miyake, *J. Am. Chem. Soc.*, 2007, **129**, 14271-14280.
40. R. W. Taylor, T.-C. Lee, O. A. Scherman, R. Esteban, J. Aizpurua, F. M. Huang, J. J. Baumberg and S. Mahajan, *ACS Nano*, 2011, **5**, 3878-3887.
41. I. Blakey, Z. Merican and K. J. Thurecht, *Langmuir*, 2013, **29**, 8266-8274.
42. Q. Dai, J. G. Worden, J. Trullinger and Q. Huo, *J. Am. Chem. Soc.*, 2005, **127**, 8008-8009.
43. L. Polavarapu and Q. H. Xu, *Langmuir*, 2008, **24**, 10608-10611.
44. P. Dey, I. Blakey, K. J. Thurecht and P. M. Fredericks, *Langmuir*, 2014, DOI: 10.1021/la4047462.
45. A. W. Bosman, H. M. Janssen and E. W. Meijer, *Chem. Rev.*, 1999, **99**, 1665-1688.
46. B. Pan, F. Gao, L. Ao, H. Tian, R. He and D. Cui, *Colloid. Surface. A*, 2005, **259**, 89-94.
47. B. Liu, A. Kazlaucinas, J. T. Guthrie and S. Perrier, *Macromolecules*, 2005, **38**, 2131-2136.
48. K. J. Thurecht, I. Blakey, H. Peng, O. Squires, S. Hsu, C. Alexander and A. K. Whittaker, *J. Am. Chem. Soc.*, 2010, **132**, 5336-5337.
49. J. H. Tan, N. A. J. McMillan, E. Payne, C. Alexander, F. Heath, A. K. Whittaker and K. J. Thurecht, *J. Polym. Sci. Pol. Chem.*, 2012, **50**, 2585-2595.
50. K. Münnemann, M. Kölzer, I. Blakey, A. K. Whittaker and K. J. Thurecht, *Chem. Commun.*, 2012, **48**, 1583-1585.
51. B. M. Ross, J. R. Waldeisen, T. Wang and L. P. Lee, *Appl. Phys. Lett.*, 2009, **95**, 193112.
52. D. S. Sebba, J. J. Mock, D. R. Smith, T. H. LaBean and A. A. Lazarides, *Nano Lett.*, 2008, **8**, 1803-1808.
53. C. Wang, Y. Du, Q. Wu, S. Xuan, J. Zhou, J. Song, F. Shao and H. Duan, *Chem. Commun.*, 2013, **49**, 5739-5741.
54. P. Yu, X. Wen, Y.-R. Toh, Y.-C. Lee and J. Tang, *RSC Adv.*, 2013, **3**, 19609-19616.
55. G. Frens, *Nature*, 1973, **241**, 20-22.
56. J. Turkevich, P. C. Stevenson and J. Hillier, *J. Phys. Chem.*, 1953, **57**, 670-673.
57. A. S. Duwez, P. Guillet, C. Colard, J. F. Gohy and C. A. Fustin, *Macromolecules*, 2006, **39**, 2729.
58. S. Zhang, K. L. Chandra and C. B. Gorman, *J. Am. Chem. Soc.*, 2007, **129**, 4876-4877.
59. J. Chiefari, Y. K. Chong, F. Ercole, J. Krstina, J. Jeffery, T. P. T. Le, R. T. A. Mayadunne, G. F. Meijs, C. L. Moad, G. Moad, E. Rizzardo and S. H. Thang, *Macromolecules*, 1998, **31**, 5559-5562.
60. P. K. Jain, K. S. Lee, I. H. El-Sayed and M. A. El-Sayed, *J. Phys. Chem. B*, 2006, **110**, 7238-7248.
61. C. Song, P. Wang and H. A. Makse, *Nature*, 2008, **453**, 629-632.
62. Z. Merican, T. L. Schiller, C. J. Hawker, P. M. Fredericks and I. Blakey, *Langmuir*, 2007, **23**, 10539-10545.
63. M. Han, X. Gao, J. Z. Su and S. Nie, *Nat. Biotechnol.*, 2001, **19**, 631-635.
64. M. Gellner, K. Kömpe and S. Schlücker, *Anal. Bioanal. Chem.*, 2009, **394**, 1839-1844.
65. J. L. West and N. J. Halas, *Annu. Rev. Biomed. Eng.*, **5**, 285-292.
66. E. C. Dreaden, M. A. Mackey, X. Huang, B. Kangy and M. A. El-Sayed, *Chem. Soc. Rev.*, 2011, **40**, 3391-3404.